Eur. Phys. J. A **30**, 31–46 (2006)
DOI 10.1140/epja/i2006-10101-2

THE EUROPEAN PHYSICAL JOURNAL A

Systematics of stopping and flow in Au+Au collisions

A. Andronic[1], J. Łukasik[1,2,a], W. Reisdorf[1], and W. Trautmann[1]

[1] GSI, D-64291 Darmstadt, Germany
[2] IFJ-PAN, Pl-31342 Kraków, Poland

Received: 27 April 2006 /
Published online: 6 October 2006 –

Abstract. Excitation functions of flow and stopping observables for the Au+Au system at energies from 40 to 1500 MeV per nucleon are presented. The systematics were obtained by merging the results of the INDRA and FOPI experiments, both performed at the GSI facility. The connection to the nuclear equation of state is discussed.

PACS. 25.70.-z Low and intermediate energy heavy-ion reactions – 25.75.Ld Collective flow – 25.70.Mn Projectile and target fragmentation

1 Introduction

The study of collective flow in nucleus-nucleus collisions has been an intense field of research for the past twenty years [1, 2]. At beam energies below several GeV per nucleon, it is mainly motivated by the goal to extract the equation of state (EoS) of nuclear matter from the quantitative comparison of measurements with the results of microscopic transport model calculations [3–5]. Considerable progress has been made in this direction in recent years but the constraints on the EoS obtained so far remain rather broad [5, 6].

The results of flow measurements performed before 1999 have been extensively reviewed in refs. [1, 2]. In the meanwhile, a variety of new results has become available regarding the directed [7–27] and elliptic [22–33] flow. These recent experiments have expanded the study of flow over a broader range of incident energies. New results became available on collective motion of produced particles [12–15]. Several studies have focussed on balance (or transition) energies associated with sign changes of a flow parameter [20–22,28–31]. High-statistics measurements allowed to explore the transverse momentum dependence of flow [17–19, 27, 28].

Since flow is generated by pressure gradients, it is clear that its quantitative study reveals aspects of the EoS. However, by itself, flow is not sufficient to fix the EoS. We need to know, as a function of beam energy, what density was achieved in the collision. An optimal condition that matter be piled up to form a dense medium, is that the two colliding ions be stopped in the course of the collision, before the system starts to expand. Information on the stopping can be obtained by studying the rapidity density distributions of the ejectiles in both the beam direction (the original direction) and the transverse direction. Recently [7], the ratio of the variances of the transverse to the longitudinal rapidities was proposed as an indicator of the degree of stopping and it was found to correlate with flow provided the incident energy E/A exceeded $150A$ MeV. While this flow-stopping correlation is only indirectly connected to a pressure-density correlation, it represents a potentially interesting constraint for microscopic simulations tending to extract the EoS from heavy-ion data.

The main purpose of this review is to present the excitation functions of flow (directed and elliptic) and of stopping in ^{197}Au + ^{197}Au collisions. This heavy, symmetric system has been studied with a variety of detectors in the intermediate energy domain throughout the last two decades:

Experiment	Reference	E/A (MeV)
PLASTIC-BALL	[34–37]	150–1050
MSU-ALADIN	[38–40]	100–400
LAND-FOPI	[41]	400
FOPI	[28, 30, 42]	90–1500
EOS	[43]	250–1150
MULTICS-MINIBALL	[44, 45]	35
MSU-4π	[20]	25–60
INDRA-ALADIN	[22, 46, 47]	40–150
CHIMERA	[48]	15

The phase space coverage and the range of observables reported in these studies vary considerably. All these data sets could be and, in most cases, were indeed used for flow studies. However, except for the comparative study

[a] e-mail: j.lukasik@gsi.de

between the Plastic Ball and the EOS data on directed flow [43], and between the Plastic Ball, the FOPI and the INDRA data on elliptic flow [22,30], no detailed comparison has been made so far, in this energy domain, of the results obtained by different experimental groups with different detectors.

In this work we will concentrate on the results obtained with the 4π FOPI and INDRA detector systems in experiments performed at the heavy-ion synchrotron SIS at GSI Darmstadt [7,18,22,28]. The covered ranges of incident energies were $90A$ MeV to $1.5A$ GeV in the FOPI and $40A$ to $150A$ MeV in the INDRA experiments. By combining the results obtained with the two detectors, having well-adapted designs for the two different energy regimes, we were able to construct coherent systematics revealing a remarkable evolution of flow and stopping over a large range of incident energies.

The observed agreement in the overlap region will serve as a measure of the absolute accuracy of the experimental data. We will focus on two aspects in this context, the systematic errors associated with the unavoidable deficiencies of the experimental devices and on the systematic errors resulting from the analysis methods which are not necessarily independent of the former. Since the two detectors have different acceptances and the reaction mechanism evolves in the energy region covered by the two experiments, particular attention will be given to the problem of impact-parameter selection and to the corrections for the reaction plane dispersion, which need to be adapted accordingly. For the latter a new method has been devised and applied to the INDRA data.

2 The detectors

The INDRA detector is constructed as a set of 17 detection rings with azimuthal symmetry around the beam axis. The most forward ring ($2^\circ \leq \theta_{lab} \leq 3^\circ$) consists of 12 Si (300 μm) – CsI(Tl) (15 cm long) telescopes. The angular range from 3° to 45° is covered by 8 rings of 192 telescopes in total, each with three detection layers: ionization chambers (5 cm of C_3F_8 at 50 mbar), Si detectors (300 μm) and CsI(Tl) scintillators with lengths decreasing from 13.8 cm to 9 cm with increasing angle. The remaining 8 rings, covering the region $45^\circ \leq \theta_{lab} \leq 176^\circ$, have two detection layers: ionization chambers (5 cm of C_3F_8 at 30 mbar) and CsI(Tl) scintillators (7.6 to 5 cm). The total granularity is 336 detection cells covering 90% of the 4π solid angle.

In the forward region ($\theta_{lab} \leq 45^\circ$), ions with $5 \leq Z \leq 80$ are identified using the $\Delta E - E$ method. Over the whole angular range, isotope identification is obtained for $1 \leq Z \leq 4$ using the technique of pulse-shape discrimination for the CsI(Tl) signals. A complete technical description of the detector and of its electronics can be found in [49], details of the calibrations performed for the GSI experiments are given in [47,50].

The FOPI detector [42,51] is comprised of two main components: the forward Plastic Wall and the Central Drift Chamber, covering regions of laboratory polar angles of $1.2^\circ < \theta_{lab} < 30^\circ$ and $34^\circ < \theta_{lab} < 145^\circ$, respectively. The Plastic Wall consists of 764 individual plastic scintillator units. Detected reaction products are identified according to their atomic number, up to $Z \simeq 12$, using the measured time-of-flight (ToF) and specific energy loss. Particles detected with the Central Drift Chamber ($Z \leq 3$) are identified according to their mass (A) by using the measured magnetic rigidity and specific energy loss. The 3-dimensional tracking profits from a high equivalent detector granularity. At beam energies of $400A$ MeV and above, the forward drift chamber Helitron can be employed for mass identification of light fragments ($Z \leq 2$) at angles $7^\circ < \theta_{lab} < 29^\circ$.

The FOPI detector has an effective granularity exceeding that of INDRA by about a factor of 4, a property matched to the increasing multiplicity of charged particles with rising beam energy[1]. Both, INDRA and FOPI detectors are essentially blind to neutral particles, such as neutrons, π^0 and γ's. The higher granularity is, however, not the only feature helping to cope with higher energies. As the energy of the emitted particles rises, a level is reached where the principle of stopping the particle in a sensitive detecting material in order to determine its energy is no longer adequate because the material depth needed leads to a high probability of nuclear reactions undermining the energy measurement. To avoid this difficulty, one switches to time-of-flight and magnetic rigidity (in addition to energy loss) measurements: the apparatus becomes larger and is no longer under vacuum. Hence the detection thresholds for the various ejectiles are raised. For the FOPI detectors this means that, *e.g.*, at $90A$ MeV fragments with $Z > 6$ cannot be detected at midrapidity anymore.

3 Impact parameter

In a binary collision of massive "objects", the transfer of energy, momentum, angular momentum, mass etc. between the two partners will be strongly affected by the impact parameter b. As a consequence, one expects to observe large event-to-event fluctuations due to impact parameter mixing. To be meaningful, a comparison of experimental observations among each other or with the predictions of theoretical simulations has to be performed for well defined and sufficiently narrow intervals of impact parameter. Generally, in microscopic physics and, in particular, in nuclear physics, the impact parameter is not directly measurable but has to be estimated from *global* observables g characterizing the registered events. Global observables are determined using all or a significant fraction of the detected particles.

The basic, so-called geometrical model assumption [52], underlying the association of an impact param-

[1] The 4π-integrated charged-particle multiplicities in central collisions increase from typically about 40 at $40A$ MeV to 95 at $150A$ MeV and exceed 200 (with one quarter of them being charged pions) at $1.5A$ GeV.

eter b with an observed value g is that g changes strictly monotonically with b allowing to postulate

$$\int_g^\infty \frac{\mathrm{d}\sigma(\bar{g})}{\mathrm{d}\bar{g}}\mathrm{d}\bar{g} = \pi b^2(g) \quad \text{or} \quad \int_0^g \frac{\mathrm{d}\sigma(\bar{g})}{\mathrm{d}\bar{g}}\mathrm{d}\bar{g} = \pi b^2(g), \quad (1)$$

where the left- (right-) hand equation holds for g decreasing (rising) with b. The distribution $\mathrm{d}\sigma(g)/\mathrm{d}g$ is determined experimentally in terms of differential cross-sections per unit of g in a minimum bias class of events, *i.e.* where a minimum number of conditions was required to trigger data taking.

At intermediate to low incident energies, especially for $E/A < 100\,\mathrm{MeV}$, the literature abounds with an impressive diversity in the choice of global observables that have been used in attempts to select either narrowly constrained impact parameters (keywords "highly exclusive" or "ultracentral") or events of special interest (keywords "fully equilibrated", "fully evaporated", "signals of phase coexistence"). The observables vary from very simple ones like proton, neutron or total charged-particle multiplicity to more specific ones as, *e.g.*, participant proton multiplicity (N_p) [53, 54], total (E_T) [55, 56] or light charged-particle transverse kinetic energy ($E_\perp^{12}$) [57], ratio of transverse-to-longitudinal kinetic energy ($Erat$) [58,59], degree of isotropy of momenta (R) [60, 61], transverse momentum directivity (D) [62–65], longitudinal kinetic-energy fraction (E_e) [66, 67], linear momentum transfer [68], total kinetic-energy loss ($TKEL$) [69,70], average parallel velocity (V_{av}) [71], midrapidity charge (Z_y) [72], total charge of $Z \geq 2$ products (Z_{bound}) [73, 74], longitudinal component of the quadrupole moment tensor (Q_{zz}) [75]. Even more complex observables are those obtained from sphericity [76,77], from the kinetic-energy tensor [78–80] or momentum tensor [67, 81, 82], the thrust (T) [67, 83, 84], the deflection angle of the projectile (Θ_{defl}) [85], the flow angle (Θ_{flow}) [3, 86], the location in a "Wilczyński plot" [69, 86, 87], harmonic moments (H_2) [86, 88, 89], or combined global variables (ρ) [90]. The most sophisticated methods used for impact parameter selection are based on, *e.g.*, principal component analysis (PCA) [91–93] or on neural-network techniques (NN) [94–96].

There are also more technical event selection schemes involving the postulation of "complete" events by demanding that nearly the full system charge or the full total linear momentum is accounted for. These latter methods are specific for a given apparatus since these observables, strictly constrained by conservation laws, would not be impact parameter selective when using a perfect detection system. In this case, a comparison of different experimental data sets at a high level of precision is difficult and a comparison with theoretical approaches must use apparatus-specific filter software that reproduces the hardware cuts causing the observed selectivity. In the present study, aiming towards joining up the data of two rather different setups, we will try to avoid using such concepts. We will restrict ourselves to the use of "simple" global observables such as total charged-particle multiplicity M_c or transverse energy $E_\perp$ or its variants $E_\perp^{12}$ (limited to $Z \leq 2$) and $Erat$ which, although it involves also the longitudinal kinetic energy, is highly correlated to $E_\perp$ due to energy conservation constraints.

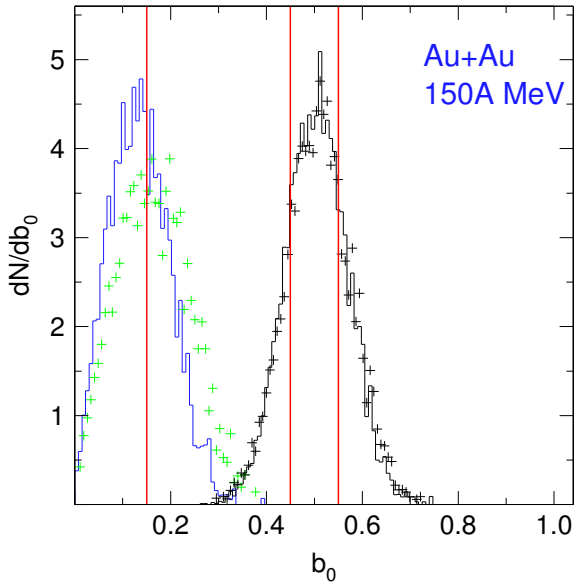

Fig. 1. Simulated reduced impact parameter distributions for Au+Au collisions at $150A\,\mathrm{MeV}$ using the global observables $Erat$ (histogram) or charged-particle multiplicity (crosses) for event selection. The two peaks correspond to nominal centralities $b_0 < 0.15$ and $0.45 < b_0 < 0.55$, respectively, as indicated by the vertical lines.

The quality of the achieved selectivity in impact parameter is illustrated in fig. 1. It shows distributions of the scaled impact parameter $b_0 = b/b_{max}$ as obtained from the IQMD transport code [97] simulations for the reaction $^{197}\mathrm{Au} + {}^{197}\mathrm{Au}$ at $150A\,\mathrm{MeV}$. We take $b_{max} = 1.15(A_P^{1/3} + A_T^{1/3})\,\mathrm{fm}$ and estimate b from the calculated differential cross-sections for the $Erat$ or multiplicity distributions, using the geometrical sharp-cut approximation. The figure gives an idea of the achievable impact parameter resolution, typically 1 to 2 fm for Au on Au, an unavoidable finite-size effect. The semi-central event class, at this energy, happens to be almost invariant against the choice of the selection method. For the central sample, about 130 mb here, the $Erat$ selection is somewhat more effective than the multiplicity selection, an observation [30] found to hold for all higher energies studied with FOPI. We also conclude that with this selection technique cross-section samples significantly smaller than 100 mb cannot be considered as representative of the chosen nominal b value.

In this simulation perfect 4π acceptance was assumed. In reality, limitations of the apparatus will further reduce the achievable selectivity. For the case of FOPI, extensive simulations suggested that the additional loss of performance is small, provided the incident energy per nucleon, E/A, is at least 150 MeV and the considered range of reduced impact parameter does not significantly exceed $b_0 = 0.5$.

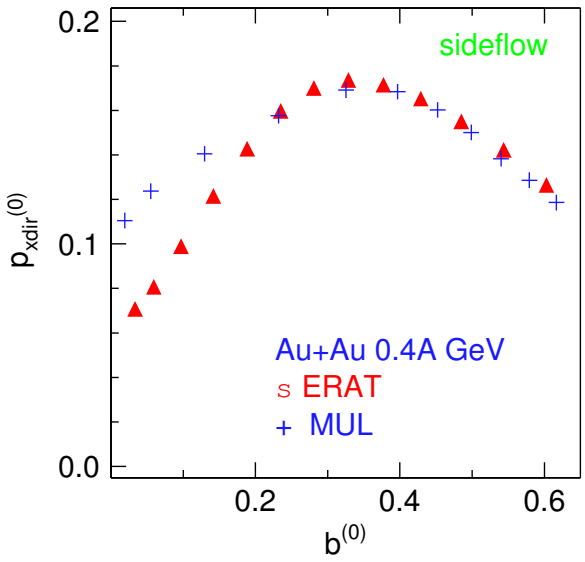

Fig. 2. Mean charge-integrated ($Z \leq 10$) scaled directed flow, $p_{xdir}^{(0)}$ measured with FOPI for Au+Au collisions at 400A MeV as a function of the scaled impact parameter b_0 as determined with *Erat* (triangles) and with the multiplicity of charged particles (crosses), after [7].

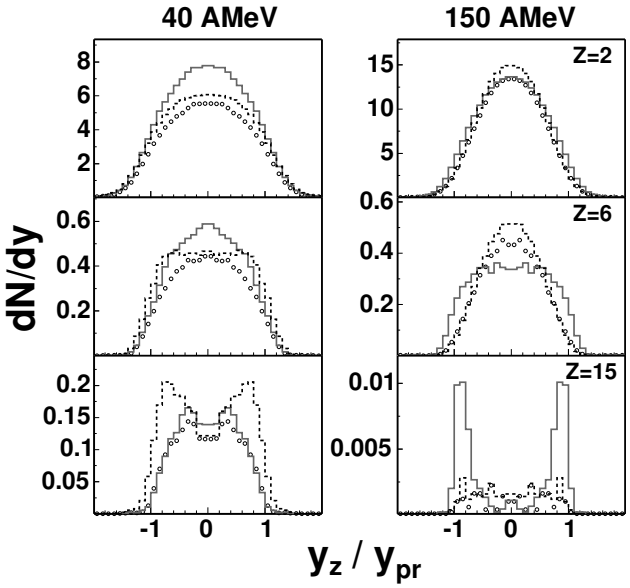

Fig. 3. Longitudinal scaled c.m. rapidity density distributions for 40A (left) and 150A (right) MeV Au+Au collisions at $b < 2$ fm from the INDRA experiment for selected charges as indicated. Solid histograms: multiplicity selection of the impact parameter, dashed histograms: *Erat*, circles: $E_\perp^{12}$.

At sufficiently high E/A, the measured directed flow can be used for a model-independent comparison of the relative performance of different selection methods. This is illustrated in fig. 2 with FOPI data for the reaction Au+Au at 400A MeV and for impact parameter selections using either *Erat* or the multiplicity of charged particles in the geometrical sharp-cut approximation.

The scaled directed flow is $p_{xdir}^{(0)} \equiv p_{xdir}/u_{1cm}$ where $p_{xdir} = \sum sign(y) Z u_x / \sum Z$ (Z fragment charge, u_{1cm} spatial part of the center-of-mass projectile 4-velocity, $u_x \equiv \beta_x \gamma$ is the transverse projection of the fragment 4-velocity on the reaction plane [98]). The sum is taken over all measured charged particles with $Z < 10$, excluding pions, and y is the c.m. rapidity. For symmetry reasons, $p_{xdir}^{(0)}$ has to converge to zero as $b_0 \to 0$. The figure, therefore, indicates that i) the b resolution is not perfect in either case and ii) for the most central collisions the *Erat* selection provides a more stringent impact parameter resolution than the multiplicity selection, as already expected on the basis of the simulations (fig. 1). The maximum value of $p_{xdir}^{(0)}$, on the other hand, and the b_0 interval where it is located are robust observables which do not significantly depend on the selection method. Based on these observations, when FOPI data is analyzed, in general one employs a mixed multiplicity-*Erat* strategy for centrality selection.

Not all global observables behave monotonically with impact parameter, as evident for p_{xdir} from fig. 2. If they are used to select central collisions, an additional cut is required to suppress the high b_0 branch. A non-monotonic behaviour can also result from losses of heavy ejectiles close to zero degree or close to target rapidity. These losses tend to increase with decreasing E/A and (or) increasing b_0. In the FOPI case we limit our analysis to $b_0 < 0.5$ and require that at least 50% of the total charge has been identified, a moderate, apparatus specific, constraint that does not significantly bias the topology of central collisions.

While for particle multiplicities the idea of a monotonic b correlation is intuitively expected, this is not self-evident for transverse energy. At sufficiently high energy ($\gtrsim$ 100A MeV), transverse energy is increasingly generated by the repeated action of many elementary collisions on the nucleonic level. Since the number of such collisions increases with increasing target-projectile overlap, high transverse energies are correlated with *low* impact parameters. If E/A is smaller than about 100 MeV mean-field effects involving the system as a whole dominate. One observes deflections of the projectile-like and target-like remnants to finite polar angles generating transverse energies that are associated with large impact parameters which carry large angular momenta. This complication can be avoided by using the sum $E_\perp^{12}$ of transverse momenta of light charged particles ($Z \leq 2$) which is more strongly related to the dissipated energy and does not involve properties of heavier fragments.

These complexities are illustrated in fig. 3 using INDRA data for Au+Au at 40A MeV and 150A MeV. Shown are charge-separated longitudinal rapidity distributions for central collisions, selected with three different observables, multiplicity, *Erat* and $E_\perp^{12}$. To the extent that stronger yield accumulations near midrapidity indicate higher centrality, the multiplicity binning is more selective of central collisions than *Erat* at 40A MeV while at 150A MeV the reverse is true. This appears more pronounced for the cases of larger fragments shown in the lower panels.

For the *Erat* and $E_\perp^{12}$ selections in fig. 3 the centrality has been defined by all the relevant reaction products except the one of interest. This method of excluding the "particle of interest" (POI) from the selection criteria allows to avoid autocorrelations between the studied observable and the one used for the estimation of centrality. On the other hand, the exclusion of the POI makes the observable used for the impact parameter selection particle dependent, *i.e.* no longer globally event dependent. This may affect the partitions belonging to a given centrality bin since, depending on the particle, the event may, or may not fulfill the criteria for a given centrality class. It has serious consequences when the autocorrelation is strong, especially for low-energy collisions which are characterized by the presence of intermediate and heavy mass fragments carrying substantial amounts of momentum. Excluding, or missing, such a fragment unavoidably affects the measure of the impact parameter and increases its fluctuations. $E_\perp^{12}$ does not depend on the exclusion or detection of heavy fragments and thus is better suited for lower energies.

On the other hand, in the case of the INDRA detector, the multiplicity observable does not seem to be the optimal centrality selector at high energies (fig. 3, right bottom panel) where due to inefficiencies for light particles (multi-hits, punch throughs), this observable may admix less central events with higher multiplicities of fragments to the most central bin. Using $E_\perp^{12}$ as a centrality selector avoids switching the selection method when studying excitation functions. As can be seen in the figure, $E_\perp^{12}$ performs similar to multiplicity at $40A$ MeV and similar to *Erat* at $150A$ MeV. Since molecular-dynamics simulations confirm this observation [99], we choose $E_\perp^{12}$ in the following as a centrality measure for the INDRA data, unless indicated otherwise.

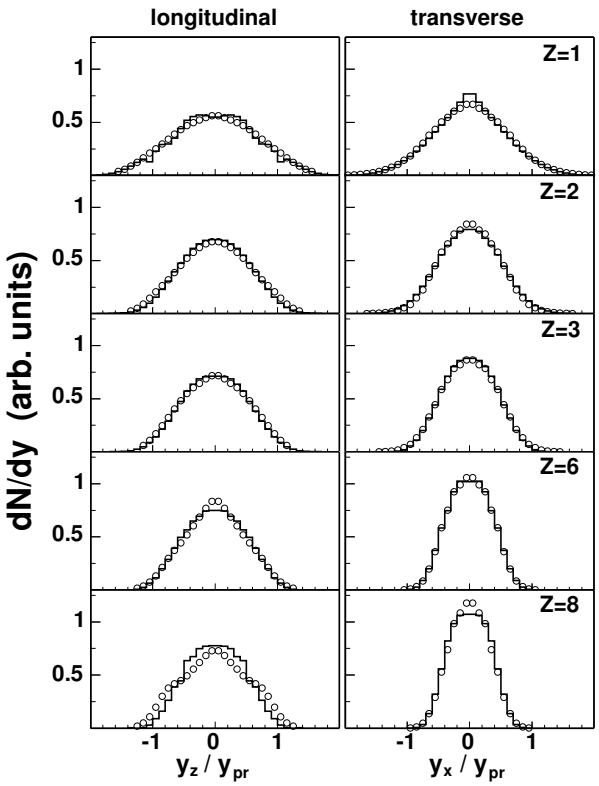

Fig. 4. Yield distributions as a function of the scaled longitudinal (left) and transverse (right) rapidity for several fragment species within $Z = 1$–8 for central Au+Au collisions at $150A$ MeV measured with FOPI (circles) and INDRA (histograms). The impact parameter $b_0 < 0.15$ is selected using *Erat* for both cases, the spectra are normalized to permit an easier comparison of their shapes.

4 Rapidity density and stopping

Rapidity distributions in longitudinal (y_z) and in an arbitrarily fixed transverse direction (y_x) as obtained with the FOPI and INDRA detectors for central Au+Au collisions at $150A$ MeV are shown in fig. 4.

To allow a closer comparison of the shapes the distributions have been normalized to the unit area, individually for each fragment charge. The *Erat* observable constructed from all detected reaction products except the particle of interest was used as impact parameter selector. In the case of the FOPI data, the distributions have been reconstructed for the uncovered phase space and symmetrized with respect to the c.m. rapidity using two-dimensional extrapolation methods [100] in the transverse momentum *vs.* rapidity plane. For $Z = 1, 2$ these corrections represent less than 10% of the total yield, for heavier fragments they amount up to 30%, leading to estimated uncertainties of 10% near midrapidity and of 5% for $|y|/y_{pr} > 0.5$. The INDRA distributions have been corrected for the 10% geometrical inefficiency [49] by multiplying the yields with a factor of 1.11. The positions of the detected particles and fragments were uniformly randomized within the active area of the detection modules. For $Z = 1$ the backward c.m. distribution was used and reflected into the forward hemisphere which is affected by losses due to punch-through of energetic particles. For heavier charges the forward part was used and symmetrized to profit from the higher granularity of the detector there and to avoid the higher thresholds affecting the yields at backward angles.

Taking into account the systematic errors (not shown in the figure), the agreement of the two independent measurements is very good. This feature is far from trivial: due to different acceptances, especially for heavier fragments, the composition of the global event selector cannot be made strictly identical for the two detectors. Since at this incident energy the difference between rapidity and velocity is small, one can say that in a naive thermal equilibrium model, ignoring flow and partial transparency effects, the two kinds of distributions, longitudinal and transverse, ought to be equal, with the common variances being a measure of the (kinetic) temperature. Clearly, this is not the case, the transverse widths are smaller than the longitudinal widths, even though the selection method, using maximal *Erat*, is definitely biased towards isolating the event sample (on the 130 mb level) with the largest

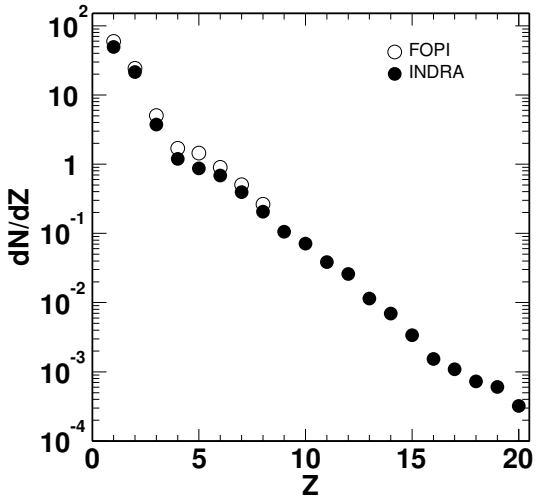

Fig. 5. Charge multiplicity distributions in central ($b_0 < 0.15$) collisions of Au+Au at 150A MeV. Open circles: FOPI data; closed circles: INDRA data.

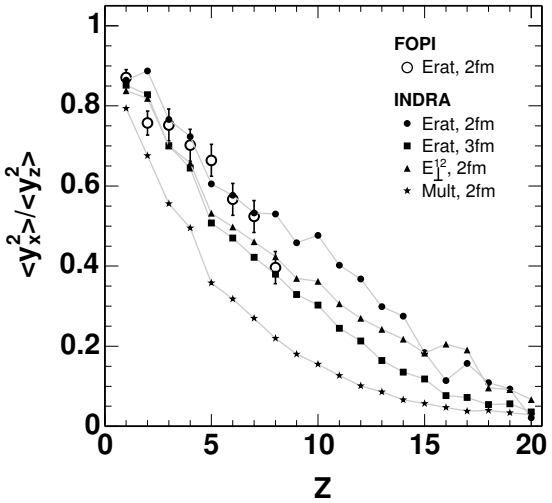

Fig. 6. Ratio of transverse to longitudinal variances for central Au+Au collisions at 150A MeV as measured with the FOPI and INDRA detectors (open and filled symbols, respectively). The variances were obtained for scaled c.m. rapidities in the range $-1 \leq y \leq 1$. The chosen selections of centrality are indicated in the legend.

ratio of transverse-to-longitudinal variances (although, as mentioned earlier, autocorrelations were removed).

The integration over rapidity yields absolute charged-particle distributions dN/dZ. The results for Au+Au at 150A MeV are shown in fig. 5. For FOPI, only $Z \leq 8$ yields are available at this energy while the INDRA data extend over almost 6 orders of magnitude up to $Z = 20$. The observed yields of heavy fragments are small, however, only about 2-3% of the available charge is clusterized in fragments with $Z > 8$, as expected at this energy where the c.m. collision energy amounts to four times the nuclear binding energy. With these 3% added, the FOPI data account for 97% of the total system charge which is consistent with the 4π-reconstruction method. The INDRA yields are systematically lower than FOPI by between 10% and 30%. The lower $Z = 1$ yield is mainly responsible for the detection of only 80% of the total system charge with INDRA but similar differences are also observed for larger Z. They are most likely caused by reaction losses and edge effects in the detectors which reduce the effective solid-angle coverage if Z identification is required. The light-particle yields may also be affected by the higher multi-hit probabilities at this incident energy at the upper end of the INDRA regime. Extrapolating these observations over the full range of incident energies studied in this work, one may expect that reaction losses and the multi-hit probability are considerably reduced at lower incident energies for INDRA while the missing yields at large Z in the FOPI case will be negligible at higher energies for the mainly central and mid-central collisions that are of interest here.

The ratio of the variances of the transverse and longitudinal rapidity distributions has recently been proposed as a measure of the degree of stopping reached in nuclear collisions [7]. The ratios obtained for central Au+Au collisions at 150A MeV, after integration over the range of scaled c.m. rapidity $-1 \leq y \leq 1$, are shown in fig. 6 as a function of Z. The open circles represent the FOPI data with error bars which include the systematic uncertainty of the reconstruction procedure. The INDRA data are shown for $Z \leq 20$ and for four different impact parameter selections as indicated in the figure.

The largest ratios from 0.8 to 0.9 are observed for light charged particles ($Z \leq 2$). With increasing fragment Z, the ratios decrease continuously to values of < 0.1 near $Z = 20$. In the common range of fragment Z and for the same impact parameter selection ($Erat, b \leq 2$ fm), the ratios measured with FOPI and INDRA are in good agreement. The selection with $Erat$ and $b \leq 3$ fm yields slightly smaller ratios as expected which, however, are similar to those obtained with $E_{\perp}^{12}$. Large transverse momenta of light charged particles and of fragments are apparently correlated. Autocorrelations are not present here because the particle of interest is removed from the impact parameter selector (see previous section). The smallest ratios of variances are obtained for selections according to multiplicity.

The trends as observed as a function of Z suggest that the heavier fragments, even in rather central collisions, experience less stopping than lighter ones and keep a strong memory of the entrance channel motion. Their transverse momenta seem to be, nevertheless, generated in collisions involving nucleons or light clusters as evident from the correlation with $E_{\perp}^{12}$. The momenta of struck nucleons absorbed in a cluster or the recoil momenta of nucleons knocked out from a cluster both contribute to their final momenta. Their relative weight will be smaller in larger fragments, consistent with the observed Z-dependence. Overall, these observations are clearly in contradiction to the assumption of global equilibrium including the kinetic degrees of freedom. Qualitatively, they agree with the pre-

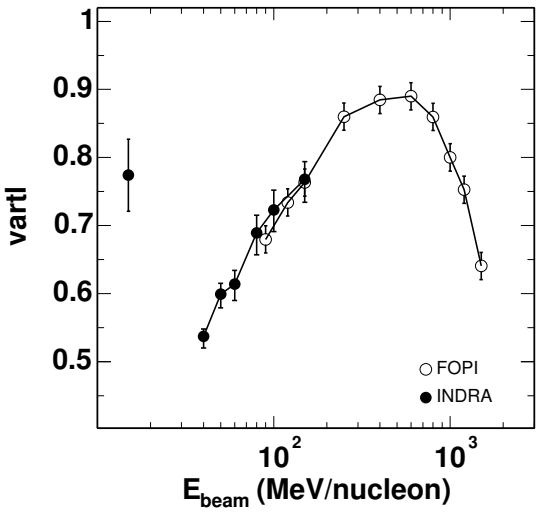

Fig. 7. Excitation function of the degree of stopping, *vartl*, in central Au+Au collisions ($b \leq 2$ fm) obtained from the FOPI (open circles) and INDRA (dots) measurements. The result at $15A$ MeV corresponds to a less central selection ($b \leq 5$ fm).

dictions of quantum molecular-dynamics calculations for fragment production in this energy range [101].

A global observable to describe stopping, *vartl*, has been introduced in ref. [7]. It is defined as the ratio of the transverse over longitudinal variances of the summed and Z-weighted rapidity distributions. The excitation function of this observable is presented in fig. 7 for central Au+Au collisions ($b \leq 2$ fm) and for the full energy range covered in the FOPI and INDRA experiments.

The FOPI results have been obtained with the *Erat* selection. The data have recently been reanalyzed by taking additional small corrections due to energy losses in structural parts of the detector into account. At the lowest three energies, this has led to an increase of *vartl* by up to about 10% compared to the data published in [7], while for the other energies the results are unaffected. The measured range of fragments extends up to $Z = 6, 8, 8$ for $E = 90A$, $120A$, $150A$ MeV, respectively. The contribution of heavier fragments to the *vartl* observable has been estimated by extrapolating their weights and variance ratios to higher Z. At $90A$ MeV this correction amounts to about 8%. The errors given in the figure are systematic and mainly reflect the uncertainty of the reconstruction procedure.

For the INDRA central event samples, the light-particle transverse energy $E_{\perp}^{12}$ has been used to select $b \leq 2$ fm for $40A$ to $150A$ MeV and $b \leq 5$ fm for the data sample at $15A$ MeV with low statistics, originally only taken for calibration purposes. For the charge-weighted average, fragments up to $Z = 60$ have been included. Except for the result at $15A$ MeV, the error bars correspond to the variation of *vartl* for centrality selections within $b \leq 1.5$ fm (upper end of the error bar) and $b \leq 2.5$ fm (lower end) and thus represent the systematic uncertainty associated with the impact parameter determination. The statistical errors are below the percent level, except at $15A$ MeV, where they are the main contribution to the error shown in the figure.

The obtained excitation function of stopping is characterized by a broad plateau extending from about $200A$ to $800A$ MeV with fairly rapid drops above and below. The highest value reached by *vartl* is about 0.9. With the INDRA data, the reduction of stopping at lower incident energies is followed down to $40A$ MeV. In the overlap region, a very satisfactory agreement within errors is observed. The measurement at $15A$ MeV suggests that stopping goes through a minimum at or below $40A$ MeV.

It is clear that only a dynamical theory will be able to reproduce this excitation function. Using the relativistic Boltzmann-Uehling-Uhlenbeck (RBUU) transport model, an analysis of the combined FOPI stopping and flow (see later) data was recently presented [102]. The input to computer codes implementing transport theoretical models are the nuclear mean field U (or EoS) and the nucleon-nucleon (nn) cross-sections σ_{nn}. Although both are not independent in a consistent theory, it is useful to consider their effects separately. In general one finds that the cross-sectional part is dominant over the mean field part for a quantitative account of the observed incomplete stopping: note that if global equilibrium, or even local equilibrium (ideal hydrodynamics), were valid cross-sections would be irrelevant. Starting at the low-energy end one qualitatively expects, when raising the energy, that the increasingly repulsive mean field (due to increasing compression) and the drop in Pauli blocking of final and intermediate states in nn scattering (due to the increasing initial rapidity gap) conspire to raise rapidly the generation of transverse energy at the expense of the longitudinal energy. At the higher-energy end (say beyond $1A$ GeV) again both aspects (mean-field and collisions) more or less may add up to make the drop faster. At $1.5A$ GeV roughly one quarter of the nucleons are excited to a resonant state. The opening up of nucleonic degrees of freedom may lead to a softening of the EoS. On the other hand, the in-medium Dirac masses M_D^* are predicted to drop substantially in covariant theories [103–105], a fact that will seriously modify the phase-space and kinematical factors influencing the elementary cross-sections [106–108]. The calculations of ref. [102] suggest that these in-medium modifications of σ_{nn} are indeed necessary to reproduce the observed stopping.

Besides the "global" information shown in fig. 7 the "particle differential" information reveals additional information on the stopping mechanisms. Figure 6 shows that the partial transparency is predominantly experienced by the heavier fragments, which presumably have survived because their constituent nucleons have suffered a less violent average collision history. This feature is also observed at the high-energy end, although the "heavy-fragment" role is played there by mass $A = 2$–4 ejectiles [109]. Restricting the stopping observable to the lightest species at the various incident energies, one obtains higher *vartl* values and flatter excitation functions. The combined role of the mean field and of in-medium modified cross-sections

will be picked up again in sect. 7 where the flow information will be added to the analysis.

5 Flow, reaction plane and corrections

Originally, the directed flow has been quantified by measuring the in-plane component of the transverse momentum [98] and the elliptic flow by parametrizing the azimuthal asymmetries using the Fourier expansion fits [110, 111]. More recently, it has been proposed [112] to express both, directed and elliptic flow in terms of the Fourier coefficients (v_1 and v_2, respectively) and also to investigate the higher flow components. The coefficients v_n are obtained by means of the Fourier decomposition [112–114] of the azimuthal distributions measured with respect to the true reaction plane:

$$\frac{\mathrm{d}N}{\mathrm{d}(\phi-\phi_R)} = \frac{N_0}{2\pi}\left(1+2\sum_{n\geq 1} v_n \cos n(\phi-\phi_R)\right) \qquad (2)$$

with ϕ_R being the azimuth of the latter. In general, the coefficients $v_n \equiv \langle \cos n(\phi-\phi_R)\rangle$ may depend on the particle type, rapidity y and the transverse momentum p_T.

The standard methods of measuring flow can be split into those using explicitly the concept of the reaction plane [98,112–114] and those based on the two-particle azimuthal correlations [115]. Still other methods have been proposed recently, satisfying the needs of high-energy experiments: the "cumulant" methods [116–118] using multiparticle correlations and the method based on the Lee-Yang theory of phase transitions [119, 120]. The latter is expected to perform well above about $100A$ MeV [119], while the three-particle variant of the "cumulant" method is claimed to be useful for extracting v_1 coefficients at energies near the balance energy and in the ultrarelativistic regime [118]. However, because the correlation methods require high event multiplicities and high-statistics data, and because the correlation between a particle and the flow vector is usually much stronger than that between two particles [121], the reaction plane methods are still more commonly used at intermediate energies. They have also been applied in the present case.

Since detectors do not allow to measure the angular momenta and spins of the reaction products, the orientation of the reaction plane can only be estimated using the momenta. The resulting azimuthal angle, ϕ_E, has a finite precision, and the measured coefficients v_n^{meas} are thus biased. They are related to the true ones through the following expression [113]:

$$v_n^{meas} \equiv \langle \cos n(\phi-\phi_E)\rangle = v_n \langle \cos n\Delta\phi\rangle, \qquad (3)$$

where the average cosine of the azimuthal angle between the true and the estimated planes, $\langle \cos n\Delta\phi\rangle \equiv \langle \cos n(\phi_R-\phi_E)\rangle$, is the required correction (also referred to as "event plane resolution" or just "resolution") for a given harmonic. Note that, since the true values of flow are obtained by dividing by the average cosine, they are always larger than the measured ones.

The literature offers many different methods to estimate the reaction plane, like the flow-tensor method [78], the fission-fragment plane [122], the flow Q-vector method [98], the transverse momentum tensor [123] (also called "azimuthal correlation" [124]) method or others [125].

Among them, the Q-vector method has received special attention. Originally, the Q-vector has been defined as a weighted sum of the transverse momenta of the measured N reaction products [98]:

$$\mathbf{Q} = \sum_{i=1}^{N} \omega_i \mathbf{p}_i^{\perp} \qquad (4)$$

with the weights ω chosen to be $+(-)1$ for reaction products in the forward (backward) c.m. hemisphere and with the possibility to exclude the midrapidity zone. The choice of the optimal weights is discussed in [72,114,117,126,127]. Definition (4) can be extended to Q-vectors built from higher harmonics [114], thus *e.g.* allowing to profit from strong elliptic flow, when applicable. Usually, in the flow studies, the POI is excluded from the sum in (4) to avoid autocorrelations. This does not concern the corrections, since the sub-events (see below) do not share particles.

The corrections for the reaction plane dispersion can be obtained using various methods [98, 112–114, 121, 123, 128–131]. What they all have in common, is the underlying assumption of the applicability of the central-limit theorem. In most of these methods the correction is searched for using the sub-event method [98], which consists in splitting randomly each event into two equal-multiplicity sub-events and getting the correction from the distribution of the relative azimuthal angle, $\Delta\Phi_{12}$, between their individual Q-vectors ("sub-Q-vectors"). This is done either by using the small-angle expansion [98] or by fitting with a theoretical distribution [113]. Instead of fitting the angular distributions one can alternatively fit the distributions of the magnitude of the total Q-vector itself [112, 114].

Assuming the Gaussian limit, ref. [113] gives an analytical formula for the distribution of $\Delta\Phi_{12}$ for the case that the distributions of sub-Q-vectors are independent and isotropic around their mean values. In refs. [112, 114] one can find the formulae relevant for the distributions of the magnitude of the Q-vector.

These methods proved their usefulness for correcting measured flow values at higher energies (see, *e.g.*, [18, 28, 98, 132, 133]) which fulfill the high-multiplicity requirement. They are, however, not adequate for the intermediate-energy reactions, below about $100A$ MeV, where the particle multiplicities are lower and the events are characterized by a broad range of masses of the reaction products. Here, the applicability of the central limit theorem for devising the corrections is less obvious.

Figure 8 illustrates the difficulties one encounters at intermediate energies. It shows the experimental distributions of $\Delta\Phi_{12}$ as measured with the INDRA detector for the Au+Au reaction at $40A$ (top) and $150A$ (bottom) MeV and for two intermediate centrality bins. The lines represent the fits obtained with the method described

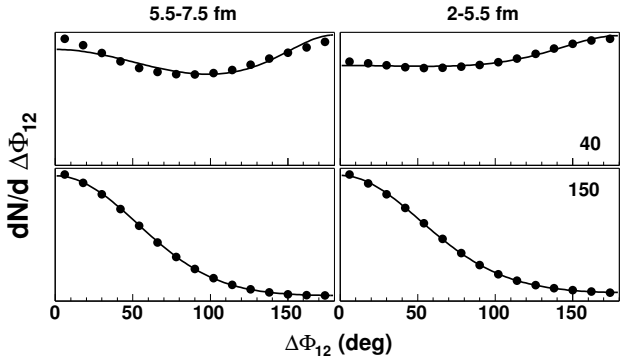

Fig. 8. Distributions of relative angle between reaction planes for two random sub-events (INDRA data, dots) and fits (lines) using the integrated product of bivariate normal distributions (eq. (5)) for centralities $b \simeq 5.5$–7.5 fm (left) and $b \simeq 2$–5.5 fm (right) and incident energies $40A$ MeV (top panels) and $150A$ MeV (bottom panels).

briefly below. The standard method [113] can, in principle, be used to derive the corrections for energies down to about $80A$ MeV, however it fails to describe distributions like those at $40A$ MeV with double maxima or maxima at backward angles, which reflect the presence and importance of the in-plane enhancement and of the correlation between sub-events.

Since at low and intermediate energies the sub-events are expected to be strongly correlated [129] and the distributions of the Q-vector no longer necessarily isotropic [113], we have extended the method of Ollitrault [113] by explicitly taking into account these two effects in the theoretical distribution of the sub-Q-vectors. The new method relies on the assumption of the Gaussian distribution of the flow sub-Q-vectors. This assumption has been verified to hold even at $40A$ MeV, except for very peripheral collisions, by performing tests with the CHIMERA-QMD model in which angular momentum is strictly conserved [134].

The form of the joint probability distribution of the random sub-Q-vectors has been searched for following the method outlined in appendix A of [121], by imposing the constraint of momentum conservation on the N-particle transverse momentum distribution and using the saddle-point approximation.

The resulting distribution has the form of a product of two bivariate Gaussians:

$$\frac{\mathrm{d}^4N}{\mathrm{d}\mathbf{Q}_1\mathrm{d}\mathbf{Q}_2} = \frac{1}{\pi^2\sigma_{sx}^2\sigma_{sy}^2(1-\rho^2)} \cdot\exp\Bigg[-\frac{(Q_{1x}-\bar{Q}_s)^2+(Q_{2x}-\bar{Q}_s)^2-2\rho(Q_{1x}-\bar{Q}_s)(Q_{2x}-\bar{Q}_s)}{\sigma_{sx}^2(1-\rho^2)} - \frac{Q_{1y}^2+Q_{2y}^2-2\rho\,Q_{1y}Q_{2y}}{\sigma_{sy}^2(1-\rho^2)}\Bigg], \quad (5)$$

where we followed the convention of [113] of including the $\sqrt{2}$ in σ; the subscripts 1, 2 refer individually and s generally to sub-events; the subscripts x and y refer to the in- and out-of-plane direction, respectively. This distribution differs from those proposed in [113, 121, 129] in that it combines all three effects that influence the reaction plane dispersion at intermediate energies, namely the directed flow (through the mean in-plane component $\bar{Q}_s$ or the resolution parameter $\chi_s \equiv \bar{Q}_s/\sigma_{sx}$ [113]), the elliptic flow (through the ratio $\alpha \equiv \sigma_{sx}/\sigma_{sy}$) and the correlation between the sub-events [129] (through the correlation coefficient $\rho \in [-1, 1]$). It reduces to the one of [113] for $\alpha = 1$ and $\rho = 0$, and to the one of [121] for $\alpha = 1$. In deriving eq. (5) it was assumed that the in- and out-of-plane correlation coefficients are equal.

Making the division into sub-events random ensures that the distributions of the sub-Q-vectors are equivalent, in particular they have the same mean values and variances. Since the total-Q-vector is the sum of the sub-Q-vectors, $\mathbf{Q} = \mathbf{Q}_1 + \mathbf{Q}_2$, one finds the following relation between the resolution parameter obtained from the distribution of the Q-vector, χ, and that obtained from the distribution of sub-Q-vectors, χ_s:

$$\chi = \chi_s\sqrt{2/(1+\rho)}\,. \quad (6)$$

Relation (6) shows how the correlation between sub-events influences the reaction plane resolution. In particular, it indicates that the resolution improves in case the sub-events are anti-correlated ($\rho < 0$), which is predicted to be the case below about $150A$ MeV except for very peripheral collisions [134].

As in [113], the joint probability distribution (5) is used after integrating it over the magnitudes of the sub-Q-vectors and one angle, leaving the $\Delta\Phi_{12}$ as the only independent variable. Unlike in [113], the resulting distribution cannot be presented in an analytical form. It depends on 3 parameters (χ_s, α, ρ) which can be obtained from fits to the experimental or model data. The quality of the obtained fits is very good, even in the non-standard cases encountered at low energies (fig. 8).

The corrections for the n-th harmonic v_n, depending now on χ and α, can be calculated (also numerically) as the mean values of the $\cos n\Delta\phi$ obtained over the total-Q-vector distribution, in a similar way as in [113]. Figure 9 shows how the elongation of the Gaussian (α), resulting from elliptic flow, modifies the corrections for the first two harmonics. It demonstrates that the in-plane emissions ($\alpha > 1$) enhance slightly the resolution for v_1 and considerably for v_2, even in the absence of the directed flow. On the other hand, squeeze-out ($\alpha < 1$) deteriorates the resolution. The figure, in particular, shows that the correction can change the sign of elliptic flow in the case of small directed flow and squeeze-out.

Since the correlation between the sub-events increases at the lower energies, the knowledge of the correlation coefficient ρ becomes crucial. Estimated values, obtained from model calculations, can be useful as constraints for ρ in the fitting procedure. For example, the CHIMERA-QMD calculations predict ρ to be around -0.43 for $40A$ MeV and $2 < b < 8$ fm and about -0.2 at $150A$ MeV. Alternatively, mean values of some rotational invariants which are derived from the measured data can be used to

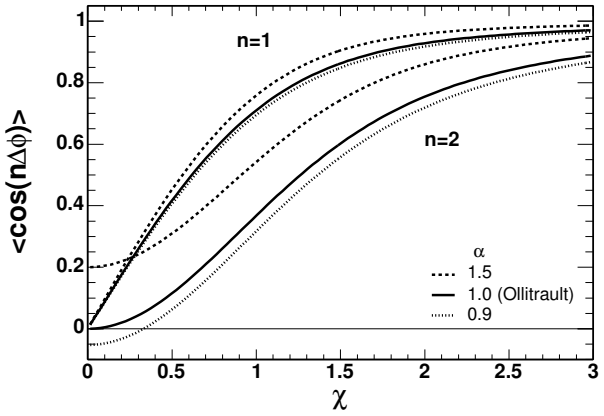

Fig. 9. Corrections for the first (3 upper curves) and the second (3 lower curves) harmonic as a function of the resolution parameter, χ, for different aspect ratios, $0.9 \leq \alpha \leq 1.5$, covering approximately the range of its variation.

reduce the number of fit parameters and to constrain the fitting routine to search for a conditional minimum [135].

Instead of fitting the azimuthal distributions one can express the probability distribution (5) in terms of the components of one of the sub-Q-vectors in the reference frame of the other, or in terms of the absolute values of the sum and of the difference of the sub-Q-vectors. The corresponding 2-dimensional experimental distributions can then be fit using such formulae. The method of fitting the distributions of components of the sub-Q-vector has been found sensitive enough to perform well without additional constraints.

The corrections obtained using various methods are presented in fig. 10. They are close to one, independent of the method, for the range of higher incident energies ($E > 100A$ MeV) where the directed flow is large and the reaction plane well defined by the high-multiplicity distribution of detected particles. At around $50A$ MeV, they go through a minimum and depend strongly on the chosen method. The FOPI flow results, as published in refs. [18, 28], have been corrected using the standard method, excluding the midrapidity region of ± 0.3 of the scaled c.m. rapidity from the Q-vector to improve the resolution. The corrections used here for the INDRA data are obtained with the new method in two ways, by fitting the azimuthal distributions and by fitting the distributions of components of the sub-Q-vectors. The mean values are given in fig. 10 (full circles) with error bars representing the systematic uncertainty as given by the difference of these results. At $15A$ MeV, the statistical errors dominate. Even at their minima, the corrections are not smaller than 0.6 and 0.5 for directed and elliptic flow, respectively, indicating that the measured flow values will increase, after applying the corrections, by no more than about a factor of two.

For a comparison of the different methods and of their applicability, also the corrections according to the standard method of Ollitrault [113] have been determined. This corresponds to fixing the parameters $\alpha = 1$ and $\rho = 0$

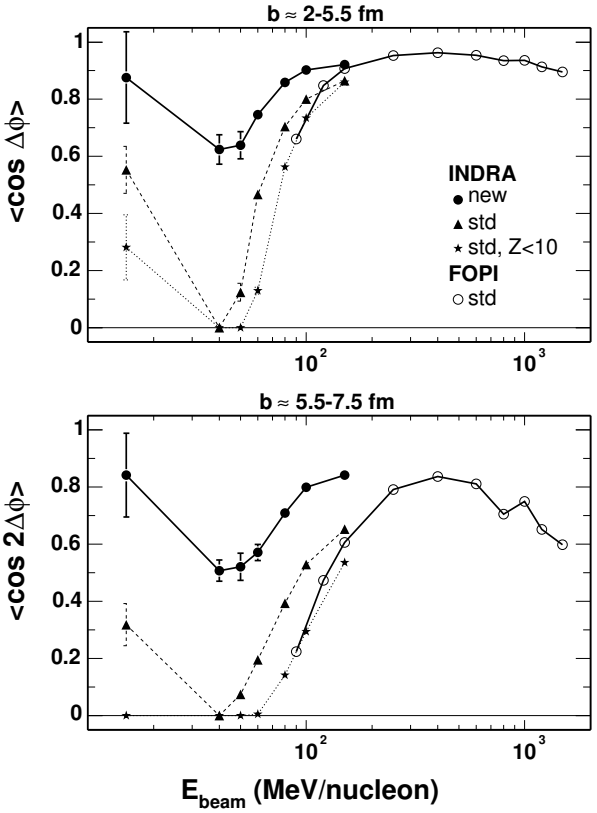

Fig. 10. Corrections for the first harmonic and impact parameter $b = 2$–5.5 fm (top) and for the second harmonic and $b = 5.5$–7.5 fm (bottom) used in the flow analysis of the Au+Au reaction. The corrections for the INDRA data (full symbols) are shown as obtained with the new method (dots, see text), with the standard (std) method (ref. [113], triangles), and with the standard method and the restriction $Z < 10$ (stars). Open circles represent the results for the FOPI data obtained with the standard method.

in the new method. Near $50A$ MeV, the results are close to zero which would require nearly infinitely large corrections (triangles in fig. 10). The figure, furthermore, shows the same corrections according to the standard method as obtained for the FOPI case (circles). They are very similar and, in the overlap region, virtually identical to the result for INDRA if the limit $Z < 10$ of the FOPI acceptance is applied in the INDRA case (stars). This very close agreement is not unexpected because good agreement was already observed for the uncorrected flow data obtained with the two detection systems [22, 28, 33]. The standard method, nevertheless, fails below about $80A$ MeV. As mentioned above, the independent, isotropic Gaussian approximation is no longer confirmed by satisfactory fits of the experimental distributions.

Several additional observations and comments can be made. Comparing the results of the new and standard methods (filled circles and triangles) shows a dramatic improvement of the resolution obtained by taking the effects of the correlation between the sub-events and of the in-plane enhancement into account. It should be stressed,

that both these effects are responsible for the finite correction for the directed flow at $40A$ MeV, near the expected balance energy [20]. Non-vanishing resolution, suggested by the new method, indicates that even here the reaction plane can be defined, and apparently, questions the occurrence of the "global" balance, which otherwise would manifest itself with the vanishing of $\langle \cos \Delta\phi \rangle$. However, the finiteness of the corrections around $40A$ MeV may also partially result from the incompleteness of the experimental data and from the mixing of events with different centralities, which may add up to mask the signal of the "global" balance. The fitting procedure yields relatively accurate results for the corrections for the first two harmonics in case of the complete results of the simulations (*e.g.*, 2–5% accuracy for $40A$ MeV and 0.2–0.4% for $150A$ MeV and $4 < b < 8$ fm [134]), and in particular, is able to reveal the signal of the "global" balance, but in the case of experimental data it will certainly return some effective corrections biased by the experimental uncertainties and inefficiencies. The effects of the latter may not necessarily drop out by applying eq. (3) to correct the measured observables, but may require additional corrections. At the higher energies, the results of the standard and the new methods approach each other but, in the overlap region of the FOPI and INDRA experiments, the differences are still significant, and need further investigation.

Comparing the less and the more complete data sets (stars and triangles, respectively) shows that the resolution improves with the completeness of the data. Triangles represent INDRA events with at least 50% of the system charge collected to which an additional single fragment carrying the missing momentum and charge was added. This artificial completion of events was found important for peripheral collisions where, due to the energy thresholds, the heavy target-like fragment is always lost. The distributions of the relative angle between sub-events become then narrowly peaked at small relative angles which improves the resolution of the reaction plane.

However, it is not only the reaction plane correction that relies on the completeness of the measured data. Also the measured v_n^{meas} parameters are affected by the non-isotropic loss of particles due to multi-hits (INDRA) or unresolved tracks in high-track-density regions (FOPI). A rough estimate of the correction [134] due to multi-hit losses for v_2 can be obtained, for segmented detectors like INDRA, by using the unfolded "true" in- and out-of-plane multiplicities and calculating the true and measured mean v_2 by integrating the azimuthal distribution (2) over the in- and out-of-plane quadrants. The "true" multiplicities can be estimated using the calculated (*e.g.*, in a way similar to that of ref. [136]) or simulated (using the detector filter and the model data) multiplicity response function specific for a given detector. An analogous procedure can be applied also for v_1; however, due to the lack of the forward-backward center-of-mass symmetry of the detector, the results may be less accurate. The flow parameters obtained from the INDRA data presented in the next section have been additionally corrected for the multi-hit losses using the above procedure. For v_1, these additional corrections vary from about 7% at $40A$ MeV to about 33% at higher energies for $Z = 1$ and do not exceed 15% for $Z = 2$. For v_2 and $Z = 1$ they increase from about 18% at $40A$ MeV to about 36% at $100A$ MeV and about 70% at $150A$ MeV, for the centrality bins in question. Within this simple procedure, the corrections depend essentially on the average of the in- and out-of-plane multiplicities and only weakly on their difference, that is why the corrections basically increase with the increasing multiplicity (thus with the centrality and incident energy). This explains the large correction factor at $150A$ MeV. Nevertheless, since v_2 is small at this energy, the absolute change of the measured value due to the correction is small compared to that at lower energies.

Generally, one may remark that, at energies below about $100A$ MeV, devising the corrections becomes a delicate task. The corrections are no longer those in the usual sense, say, of a few percent. Depending on the method, they may change the measured results by a large factor, mainly because of the smallness of directed flow around $40A$–$50A$ MeV. The accuracy relies in addition on the completeness of the data. Flow data free of reaction plane dispersions are, nevertheless, very desirable since they allow to compare the results obtained with different detectors. They are also of great interest from the theoretical point of view, by permitting the direct comparison with the model predictions. In problematic cases, however, detailed filtering of the model results and treating them with the experimental type of analysis may still be necessary, if not for the direct comparison on the level of uncorrected observables, then for the reliable estimate of the systematic uncertainties associated with the correction scheme.

The effects of momentum conservation, distortions due to removal of the particle of interest (expected to be important at low multiplicities (energies)) and possible corrections to the reaction plane resolution due to the detector inefficiencies (missing part of the Q-vector) remain a subject for future study.

6 Directed and elliptic flow

The rapidity dependence of the slope of the directed-flow $\partial v_1/\partial y$ at midrapidity for $Z = 1$ and 2 particles, integrated over transverse momentum, is shown in fig. 11. The INDRA data is combined with the FOPI data (published for $Z = 2$ in [18]), both measured for mid-central collisions with impact parameters of 2–5.5 fm and shown after correcting for the reaction plane dispersion. The FOPI data has been corrected using the method of [113] while the INDRA data has been corrected using the method outlined in sect. 5. In both data sets the reaction plane has been reconstructed using the Q-vector method with the weights $\omega = sign(y_{cm})$, excluding the POI. In case of the FOPI data the midrapidity region of ± 0.3 of the scaled rapidity has been excluded from the Q-vector to improve the resolution. The INDRA data has been corrected for the effects of momentum conservation [137]. In both cases linear fits have been performed in the range of ± 0.4 of the

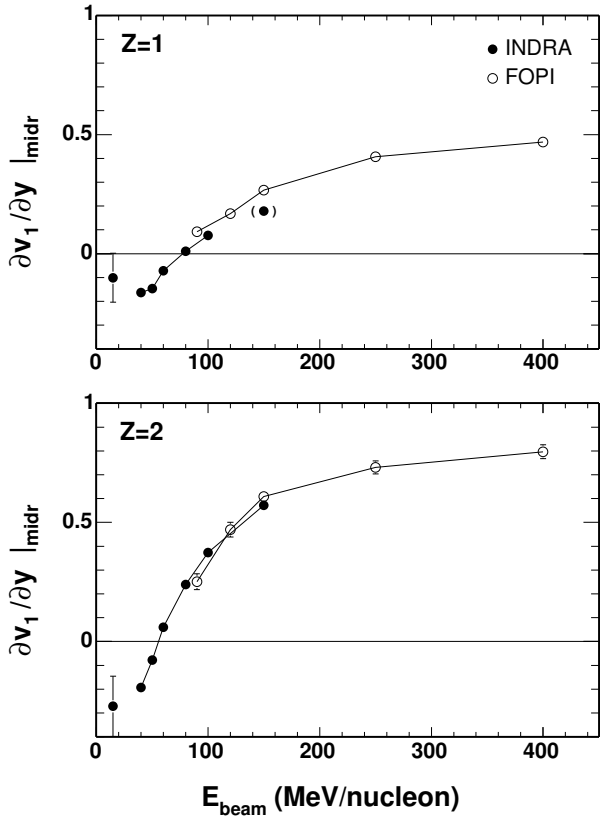

Fig. 11. Slopes of directed flow $\partial v_1/\partial y$ for $Z = 1$ (top) and $Z = 2$ (bottom) particles integrated over p_T for mid-central collisions (2–5.5 fm). The open and filled symbols represent the FOPI [18] and the INDRA data, respectively. The uncertainty at 15A MeV is mainly statistical. The INDRA point, in brackets, at 150A MeV in the top panel is biased due to experimental inefficiencies for $Z = 1$ at this energy.

scaled c.m. rapidity, except for the 15A MeV data where the range of ± 0.55 was used.

The excitation function of the slope of the directed flow at midrapidity for $Z = 1$ changes sign around 80A MeV. The apparent minimum around 40A MeV is mostly suggested by the 15A MeV data point and should be confirmed by other measurements. The FOPI data has been additionally corrected for the effects of unresolved tracks in the in-plane high-track-density region. This correction influences also the slope of the v_1 rapidity distribution, increasing it by up to 15% for $Z = 1$ and up to 5% for $Z = 2$. The INDRA results have been corrected for the effect of multi-hit losses (see sect. 5). The still apparent discrepancy between the INDRA and FOPI results at 150A MeV can be partially attributed to the losses of $Z = 1$ particles due to punch-through effects in the INDRA detector at high energies. Up to 10% of the difference may also come from the different methods used for correcting the reaction plane dispersions (see fig. 10).

For $Z = 2$, the slope of v_1 is seen to rise monotonically with energy over the full range of 15 to 400 MeV per nucleon which is covered by the two experiments. Here, the agreement in the overlap region is slightly better reflecting the better efficiency of the INDRA detector for $Z = 2$ particles. The trends observed for the uncorrected data [22] for v_1 are preserved. Unlike in ref. [20], the excitation function does not show a clean signature of a minimum (see ref. [22] for discussion). It changes sign between 50 and 60 MeV per nucleon, in agreement with the extrapolated values of the balance energy, E_{bal}, obtained from the higher-energy measurements [43,138,139].

Negative flow is observed not only for $Z = 1, 2$ (fig. 11) but with even larger slopes also for other light fragments. This intriguing phenomenon has already been reported for the lighter systems $^{40}\mathrm{Ar} + {}^{58}\mathrm{Ni}$, $^{58}\mathrm{Ni} + {}^{58}\mathrm{Ni}$, and $^{129}\mathrm{Xe} + {}^{\mathrm{nat}}\mathrm{Sn}$, provided the "1-plane-per-particle" method was used for estimation of the reaction plane [21]. For these systems, a balance energy has been determined by associating it with the minima of the approximately parabolic excitation functions of the flow parameter which, in the cases of $^{40}\mathrm{Ar} + {}^{58}\mathrm{Ni}$ and $^{58}\mathrm{Ni} + {}^{58}\mathrm{Ni}$, appeared at negative flow values. Negative flow values of light reaction products can indeed be measured experimentally, provided the detector is able to measure "quasi-complete" events, including the heavy fragments. Then, the observed anti-flow of light products is measurable relative to the reaction plane fixed and oriented by the heavy remnants.

A possible scenario of the anti-flow has been proposed for the lighter systems in [21], and for the heavy systems, emphasizing the role of the strong Coulomb field, in [22]. Despite the appeal of a globally defined balance energy, it is worth noticing that directed flow apparently never vanishes completely. It was shown with BUU calculations that at the balance energy the flow cancellation results from a complex transverse momentum dependence and that the flow pattern is influenced by EoS and σ_{nn} [140]. The presently available differential data, measured by FOPI down to 90A MeV [18] suggest that the change of sign of v_1 is dependent, in addition to transverse momentum, also on particle type and rapidity.

The results on v_2 measured at midrapidity are summarized in fig. 12. Elliptic flow varies as a function of energy from a preferential in-plane, rotational-like [141–143], emission ($v_2 > 0$) to an out-of-plane, or "squeeze-out" [37] ($v_2 < 0$) pattern, with a transition energy of about 150A MeV. This transition energy is larger than that for the directed flow (see above and the discussion in ref. [139]) and was shown to depend on centrality, particle type and transverse momentum [28,30]. For higher energies, the strength of the collective expansion overcomes the rotational-like motion, leading to an increase of out-of-plane emission. A maximum is reached at 400A MeV, followed by a decrease towards a transition to preferential in-plane emission [29,144]. This behavior is the result of a complex interplay between fireball expansion and spectator shadowing [28], with the spectators acting as clocks of the expansion times. For instance, in the energy range 400A–1500A MeV, the passing time of the spectators decreases from 30 to 16 fm/c, implying that overall the expansion gets about two times faster in this energy range. This interpretation is supported by the observed

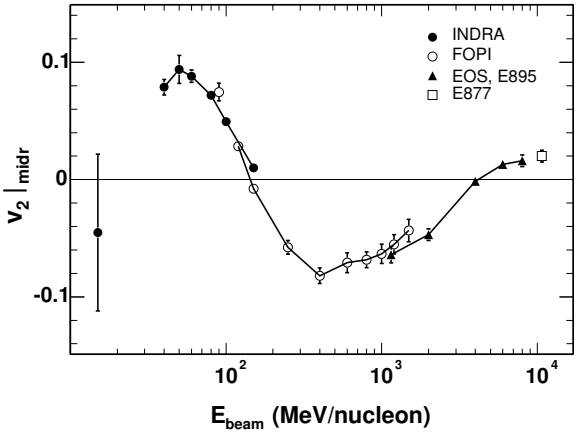

Fig. 12. Elliptic flow parameter v_2 at mid-rapidity for collisions at intermediate impact parameters (about 5.5–7.5 fm) as a function of incident energy, in the beam frame. The filled and open circles represent the INDRA and FOPI [28] data, respectively, for $Z = 1$ particles, the triangles represent the EOS and E895 [29] data for protons and the square represents the E877 data [144] for all charged particles.

scaling of elliptic flow as a function of transverse momentum scaled with beam momentum [28]. We note that the energy dependence of elliptic flow is similar to that of directed flow [1,2,7], with the extra feature of the transition to in-plane flow at $4A$ GeV [29]. This high-energy transition has received particular interest as it is expected to provide a sensitive probe of the EoS at high densities [145]. At SPS and RHIC energies, the in-plane elliptic flow is determined by the pressure gradient-driven expansion of the almond-shaped isolated fireball [146] and is currently under intensive experimental investigation [147–149].

The agreement between the corrected INDRA and FOPI data is good. The INDRA results have been corrected using the new method, including the correction for the multi-hit losses (see sect. 5). According to IQMD calculations, the reaction plane correction for the lowest FOPI energy of $90A$ MeV appears to be somewhat overestimated. On the other hand, this may partially compensate for the lack of corrections due to unresolved tracks which were not applied for v_2 in the FOPI case. Overall, the differences between the corrections is small enough, so that comparisons of uncorrected data sets are already meaningful. A good agreement was found to exist for the INDRA [22,33], FOPI [28] and Plastic Ball [37] data in the reference frame of the directed flow and without the correction for reaction plane resolution [28,33].

A remarkable feature of the v_2 observable is that it allows to show a continuous evolution over a region covering completely different reaction mechanisms, from those dominated by the mean field near the deep inelastic domain, and the multifragmentation in the Fermi energy domain towards the participant-spectator regime at relativistic energies.

7 Correlation between stopping and flow

Information on stopping and flow in heavy-ion collisions represents part of the input to theoretical efforts to deduce constraints on the EoS. Remembering that the EoS is a relation between pressure and density, it is intuitively understandable that these two heavy-ion observables are related to the EoS: flow is generated by pressure gradients established in compressed matter, while the achieved density is connected to the degree of stopping. Recently, it was observed [7] that a strong correlation exists between the stopping, measured in central collisions and the directed flow measured at impact parameters where it is maximal (see fig. 2). The relevant data are shown in fig. 13 in the upper left panel. Plotted against each other are two dimensionless global event observables characterizing stopping, *vartl*, and global scaled directed flow, $p_{xdir}^{(0)}$, both defined earlier.

The data points correspond to 21 system energies with varying system size (from Ca+Ca to Au+Au) and energy (from $150A$ to $1930A$ MeV). The straight correlation line represents a linear least-squares fit to the data and is repeated in the other panels. These other panels show the location along the correlation line of theoretical simulations using the IQMD code for Au+Au at $400A$, $1000A$ and $1500A$ MeV as indicated. The points are marked HM and SM, respectively, for a stiff (incompressibility $K = 380$ MeV) and a soft ($K = 200$ MeV)

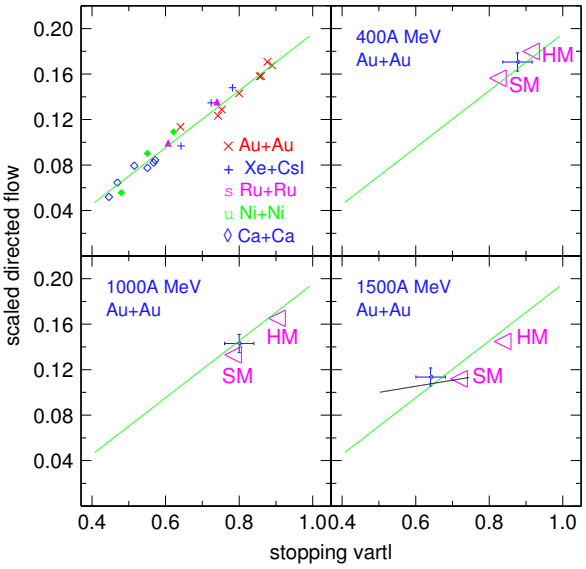

Fig. 13. Upper left panel: Correlation between the maximal directed sideflow and the degree of stopping, after [7]. The line is a linear least-squares fit to the data, which extend from $0.15A$ to $1.93A$ GeV. The correlation line is repeated in the other panels which show results of simulations for Au+Au at three incident energies using two different equations of state, SM and HM, together with the experimental points. The short segment passing through the SM point in the lower right panel shows an estimate of the trajectory using the SM EoS and modifying the in-medium cross-sections in a way that is compatible with [102].

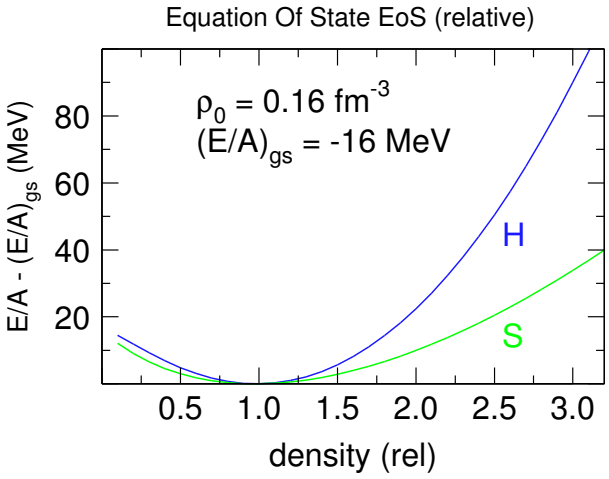

Fig. 14. Equations of state (relative to the ground state) used in the calculation.

EoS. The M in HM and SM stands for the momentum dependence of the nn interaction. IQMD incorporates a phenomenological Ansatz fitted to experimental data on the real part of the nucleon optical potential. The relevant experimental points are given together with their estimated systematic errors (these errors were omitted for clarity in the upper left panel, but are of comparable magnitude for all the data). The main purpose is to show the sensitivity of these combined observables to variations of the zero-temperature EoS as compared to the uncertainty of the data. The EoS, that are purely technical, are shown in fig. 14. The trajectory of the simulation when changing K seems to follow the correlation line, the distance between SM and HM is larger at $1000A$ MeV than at $400A$ MeV (*i.e.* the sensitivity is increased at the higher energy), but then does not seem to further increase at the highest energy, possibly due to the increase of transparency suggested by fig. 7. Data measured at energies below $150A$ MeV do not continue the same linear correlation, an interesting topic that deserves further studies.

In our exploratory IQMD simulations [97,150] we have not tried to be realistic with regard to in-medium modifications of the nucleon-nucleon cross-sections σ_{nn}, using instead the vacuum values standardly implemented in the code [97]. An estimate of the trajectory in the flow *versus* stopping plot when the EoS is kept constant, but the σ_{nn} are decreased is shown in the right-hand lower panel of fig. 13. For this estimate we rely on the more sophisticated calculations of ref. [102] which show that a switch to more realistic smaller σ_{nn} decreases the stopping by about 20% and the scaled sideflow by 6–7%, *i.e.* σ_{nn} acts more strongly, relatively speaking, on the stopping than on the scaled flow, as expected. The σ_{nn} modification trajectory crosses the correlation line because it has a different, flatter, slope than the EoS modification trajectory joining the SM to the HM point (which is not plotted) which happens to have a slope very similar to that of the experimental correlation line. Generally speaking, one can say that an underestimation of the apparent transparency will lead to an underestimation of the stiffness of the EoS. Nevertheless, the procedure just outlined suggests that an EoS closer to SM than HM would seem to be more appropriate to describe the data. The same conclusion was reached from the comparison of the FOPI data on directed flow, including its p_T-dependence, to IQMD calculations [19] and from the comparison of the out-of-plane expansion to BUU calculations [32].

Despite this encouraging result we would like to stress at this time that it would be premature to draw firm conclusions from one particular transport code and it is beyond the scope of this experimental contribution to the subject to conclusively settle the question of the EoS. Besides trying to predict correctly the global observables just shown, probably a good strategy to start with, the simulations must then proceed to reproduce the more differential data such as the variations of the stopping and of the various flow components with the particle type, as shown here in figs. 6 and 11, respectively. Another important physics quantity one would like to have under theoretical control, in order to be convincing on the conclusion side, is the created entropy. Although this is not a direct observable, the entropy at freeze-out is strongly constrained by the degree of clusterization (of which we showed an example in fig. 5) and the degree of pionization. An idea of the freeze-out volume can be obtained from two-particle correlations [151], or even multi-particle correlations [152,153]. All this is a rather challenging task. We refer to the work of Danielewicz, Lacey and Lynch [5] for a summary of the situation obtained a few years ago using a subset of the then available heavy-ion data reaching up to the AGS energies.

8 Summary and outlook

We have presented a systematics of directed and elliptic flow and of stopping for $^{197}\mathrm{Au} + {}^{197}\mathrm{Au}$ reactions in the intermediate range of energies from 40 to 1500 MeV per nucleon by merging the data from INDRA and FOPI experiments performed at the SIS synchrotron at GSI. The overlap region of the two data sets, 90 to 150 MeV per nucleon incident energy, has been used to confirm their accuracy on an absolute scale, and a very satisfactory agreement has been found.

Particular emphasis was given to the experimental reconstruction of the impact parameter and to the corrections required by the dispersion of the reconstructed azimuthal orientation of the reaction plane. The superiority of observables based on transverse energy, either the ratio $Erat$ of transverse to longitudinal energy or the transverse energy $E_\perp^{12}$ of light charged particles with $Z \leq 2$, over multiplicity for the selection of central collisions has been demonstrated. A new method, derived by extending the Gaussian approximation of the sub-Q-vector distributions to the non-isotropic case and by including the effect of correlation between the sub-events, has been presented and applied to the data at the lower incident energies at which the multiplicities are still moderate and the range of emitted fragment Z is still large, even in the most central collisions. The differences between the standard and the

new corrections of derived flow parameters are significant up to incident energies as high as 150 MeV per nucleon.

The deduced excitation functions of the v_1 and v_2 observables describing directed and elliptic flow exhibit several changes of sign which reflect qualitative changes of the underlying dynamics as a function of the bombarding energy. The transition from mean-field–dominated attractive sidewards flow to repulsive dynamics is observed for $Z = 1$ and $Z = 2$ particles at 80 MeV and 60 MeV per nucleon, respectively, in mid-central collisions. The transition from predominantly in-plane to out-of-plane emissions occurs at 150 MeV per nucleon for $Z = 1$ particles. The second change of sign at several GeV per nucleon marks the transition to the ultrarelativistic regime. These transition points are quite well established and not very sensitive to the chosen correction method. The present study shows that also the maxima reached by the flow parameters are reliable within the typically 5% systematic uncertainties due to the corrections and the impact parameter selection. Within this margin they may be used to test transport model predictions and their sensitivity to the chosen parameterization of the nuclear EoS.

It has, furthermore, been shown that the significance of the comparison can be enhanced by including the experimentally observed stopping as represented by the ratio of the variances of the integrated transverse and longitudinal rapidity distributions. This observable can best be determined for central collisions at which the directional flow vanishes for symmetry reasons whereas the compression in the collision zone presumably reaches its maximum. The common origin of the observed stopping and flow is evident from the strict correlation of the two observables, including finite-size effects. However, their individual sensitivity to the magnitude of the nucleon-nucleon cross-sections and to the flow parameters is different and can be used to resolve ambiguities between these two main ingredients of the models. The sensitivity to parameters of the equation of state is shown to increase with bombarding energy over the present energy range, and a soft EoS is clearly favored by the data.

Further constraints for the determination of the parameters of the equation of state can be obtained by including the detailed dependences of flow on the fragment Z, the impact parameter and the accepted ranges of transverse momentum and rapidity into the comparison with theory. These data, for the present reactions, are either available already or in preparation. This will have to be accompanied by theoretical studies of the still existing systematic differences between specific code realizations. The importance or necessity of full antisymmetrization at low energies or of a covariant treatment at high bombarding energies and the role of nucleonic excitations will have to be assessed.

On the experimental side, a gap of missing flow data for the Au+Au system exists at energies below 40 MeV per nucleon where interesting information on transport coefficients as, *e.g.*, shear *versus* bulk viscosity or thermal conductivity may be obtained. The origin of the observed negative flow should be confirmed and clarified. At higher energies, new information, possibly also on the symmetry part of the equation of state, can be expected from new experiments involving isotopically pure projectiles and targets and detector systems permitting mass identification at midrapidity.

The authors would like to thank Y. Leifels for the implementation of the IQMD code at GSI, the FOPI and INDRA-ALADIN Collaborations for the permission to include partially unpublished data in this comparative study, and J.-Y. Ollitrault for stimulating discussions on flow evaluation and corrections.

References

1. W. Reisdorf, H.G. Ritter, Annu. Rev. Nucl. Part. Sci. **47**, 663 (1997).
2. N. Herrmann *et al.*, Annu. Rev. Nucl. Part. Sci. **49**, 581 (1999).
3. H. Stöcker, W. Greiner, Phys. Rep. **137**, 277 (1986).
4. P. Danielewicz, Nucl. Phys. A **673**, 375 (2000).
5. P. Danielewicz *et al.*, Science **298**, 1592 (2002).
6. C. Fuchs, H.H. Wolter, *Modelization of the EOS*, this topical issue.
7. W. Reisdorf *et al.*, Phys. Rev. Lett. **92**, 232301 (2004).
8. R.C. Lemmon *et al.*, Phys. Lett. B **446**, 197 (1999).
9. M.M. Htun *et al.*, Phys. Rev. C **59**, 336 (1999).
10. E.P. Prendergast *et al.*, Phys. Rev. C **61**, 024611 (2000).
11. D.J. Magestro *et al.*, Phys. Rev. C **62**, 041603(R) (2000).
12. P. Crochet *et al.*, Phys. Lett. B **486**, 6 (2000).
13. P. Crochet *et al.*, J. Phys. G **27**, 267 (2001).
14. A. Devismes *et al.*, J. Phys. G **28**, 1591 (2002).
15. F. Uhlig *et al.*, Phys. Rev. Lett. **95**, 012301 (2005).
16. G.D. Westfall, Nucl. Phys. A **681**, 343c (2001).
17. H. Liu *et al.*, Phys. Rev. Lett. **84**, 5488 (2000).
18. A. Andronic *et al.*, Phys. Rev. C **64**, 041604 (2001).
19. A. Andronic *et al.*, Phys. Rev. C **67**, 034907 (2003).
20. D.J. Magestro *et al.*, Phys. Rev. C **61**, 021602 (2000).
21. D. Cussol *et al.*, Phys. Rev. C **65**, 044604 (2002).
22. J. Łukasik *et al.*, Phys. Lett. B **608**, 223 (2005).
23. N.N. Abd-Allah, J. Phys. Soc. Jpn. **69**, 1068 (2000).
24. L. Chkhaidze *et al.*, Phys. Lett. B **479**, 21 (2001).
25. L.J. Simić, J. Milošević, J. Phys. G **27**, 183 (2001).
26. N. Bastid *et al.*, Nucl. Phys. A **742**, 29 (2004).
27. N. Bastid *et al.*, Phys. Rev. C **72**, 011901 (2005).
28. A. Andronic *et al.*, Phys. Lett. B **612**, 173 (2005).
29. C. Pinkenburg *et al.*, Phys. Rev. Lett. **83**, 1295 (1999).
30. A. Andronic *et al.*, Nucl. Phys. A **679**, 765 (2001).
31. P. Chung *et al.*, Phys. Rev. C **66**, 021901(R) (2002).
32. G. Stoicea *et al.*, Phys. Rev. Lett. **92**, 072303 (2004).
33. J. Łukasik *et al.*, Prog. Part. Nucl. Phys. **53**, 77 (2004).
34. K.G.R. Doss *et al.*, Phys. Rev. Lett. **57**, 302 (1986).
35. K.G.R. Doss *et al.*, Phys. Rev. Lett. **59**, 2720 (1987).
36. H.H. Gutbrod *et al.*, Rep. Prog. Phys. **52**, 1267 (1989).
37. H.H. Gutbrod *et al.*, Phys. Rev. C **42**, 640 (1990).
38. M.B. Tsang *et al.*, Phys. Rev. Lett. **71**, 1502 (1993).
39. W.C. Hsi, Phys. Rev. Lett. **73**, 3367 (1994).
40. M.B. Tsang *et al.*, Phys. Rev. C **53**, 1959 (1996).
41. Y. Leifels *et al.*, Phys. Rev. Lett. **71**, 963 (1993).
42. J. Ritman *et al.*, Nucl. Phys. B (Proc. Suppl.) **44**, 708 (1995).
43. M.D. Partlan *et al.*, Phys. Rev. Lett. **75**, 2100 (1995).

44. M. D'Agostino *et al.*, Phys. Rev. Lett. **75**, 4373 (1995).
45. M. D'Agostino *et al.*, Phy. Lett. B **371**, 175 (1996).
46. A. Le Fèvre *et al.*, Nucl. Phys. A **735**, 219 (2004).
47. J. Łukasik *et al.*, Phys. Rev. C **66**, 064606 (2002).
48. A. Pagano, private communication; see also *Proceedings of the IWM2005 International Workshop on Multifragmentation and related topics, Catania, Italy, 2005*, edited by R. Bougault *et al.*, Conf. Proc., Vol. **91** (Italian Physical Society, Bologna, 2006).
49. J. Pouthas *et al.*, Nucl. Instrum. Methods Phys. Res. A **357**, 418 (1995).
50. A. Trzciński *et al.*, Nucl. Instrum. Methods Phys. Res. A **501**, 367 (2003).
51. A. Gobbi *et al.*, Nucl. Instrum. Methods A **324**, 156 (1993).
52. C. Cavata *et al.*, Phys. Rev. C **42**, 1760 (1990).
53. J. Gosset *et al.*, Phys. Rev. C **16**, 629 (1977).
54. K.G.R. Doss *et al.*, Phys. Rev. C **32**, 116 (1985).
55. L. Phair *et al.*, Nucl. Phys. A **548**, 489 (1992).
56. R. Pak *et al.*, Phys. Rev. C **53**, R1469 (1996).
57. J. Łukasik *et al.*, Phys. Rev. C **55**, 1906 (1997).
58. C. Kuhn *et al.*, Phys. Rev. C **48**, 1232 (1993).
59. W. Reisdorf *et al.*, Nucl. Phys. A **612**, 493 (1997).
60. H. Ströbele *et al.*, Phys. Rev. C **27**, 1349 (1983).
61. Y. Larochelle *et al.*, Phys. Rev. C **53**, 823 (1996).
62. P. Beckmann *et al.*, Mod. Phys. Lett A **2**, 163 (1987).
63. R. Bock *et al.*, Mod. Phys. Lett A **2**, 721 (1987).
64. J.P. Alard *et al.*, Phys. Rev. Lett. **69**, 889 (1992).
65. L. Phair *et al.*, Nucl. Phys. A **564**, 453 (1993).
66. G. Bertsch, A.A. Amsden, Phys. Rev. C **18**, 1293 (1978).
67. J. Cugnon, D. L'Hôte, Nucl. Phys. A **397**, 519 (1983).
68. T.C. Awes *et al.*, Phys. Rev. C **24**, 89 (1981).
69. R.J. Charity *et al.*, Z. Phys. A **341**, 53 (1991).
70. S. Piantelli *et al.*, Phys. Rev. Lett. **88**, 052701 (2002).
71. J. Pèter *et al.*, Nucl. Phys. A **519**, 611 (1990).
72. C.A. Ogilvie *et al.*, Phys. Rev. C **40**, 654 (1989).
73. J. Hubele *et al.*, Z. Phys. A **340**, 263 (1991).
74. A. Schüttauf *et al.*, Nucl. Phys. A **607**, 457 (1996).
75. W. Bauer, Phys. Rev. Lett. **61**, 2534 (1988).
76. G. Hanson *et al.*, Phys. Rev. Lett. **35**, 1609 (1975).
77. S. Brandt, H.D. Dahmen, Z. Phys. C **1**, 61 (1979).
78. M. Gyulassy *et al.*, Phys. Lett. B **110**, 185 (1982).
79. P. Danielewicz, M. Gyulassy, Phys. Lett. B **129**, 283 (1983).
80. G. Buchwald *et al.*, Phys. Rev. **28**, 2349 (1983).
81. S.L. Wu, G. Zobernig, Z. Phys. C **2**, 107 (1979).
82. J. Cugnon *et al.*, Phys. Lett. B **109**, 167 (1982).
83. E. Farhi, Phys. Rev. Lett. **39**, 1587 (1977).
84. J. Kapusta, D. Strottman, Phys. Lett. B **106**, 33 (1981).
85. G. Buchwald *et al.*, Phys. Rev. C **24**, 135 (1981).
86. J.D. Frankland *et al.*, Nucl. Phys. A **689**, 905 (2001).
87. J.F. Lecolley *et al.*, Phys. Lett. B **387**, 460 (1996).
88. G.C. Fox, S. Wolfram, Phys. Rev. Lett. **41**, 1581 (1978).
89. G.C. Fox, S. Wolfram, Phys. Lett. B **82**, 134 (1979).
90. P. Pawłowski *et al.*, Z. Phys. A **357**, 387 (1997).
91. P. Désesquelles, Ann. Phys. (Paris) **20**, 1 (1995).
92. P. Désesquelles *et al.*, Phys. Rev. C **62**, 024614 (2000).
93. E. Geraci *et al.*, Nucl. Phys. A **734**, 524 (2004).
94. S.A. Bass *et al.*, J. Phys. G **20**, L21 (1994).
95. C. David *et al.*, Phys. Rev. C **51**, 1453 (1995).
96. F. Haddad *et al.*, Phys. Rev. C **55**, 1371 (1997).
97. C. Hartnack *et al.*, Eur. Phys. J. A **1**, 151 (1998).
98. P. Danielewicz, G. Odyniec, Phys. Lett. B **157**, 146 (1985).
99. E. Plagnol *et al.*, Phys. Rev. C **61**, 014606 (2000).
100. W. Reisdorf *et al.*, Phys. Lett. B **595**, 118 (2004).
101. K. Zbiri *et al.*, preprint nucl-th/0607012.
102. T. Gaitanos *et al.*, Phys. Lett. B **609**, 241 (2005).
103. R. Brockmann *et al.*, Phys. Rev. C **42**, 1965 (1990).
104. E.N.E. van Dalen *et al.*, Phys. Rev. Lett. **95**, 022302 (2005).
105. A. Mishra *et al.*, Phys. Rev. C **69**, 024903 (2004).
106. R. Malfliet *et al.*, Prog. Part. Nucl. Phys. **21**, 207 (1988).
107. C. Fuchs *et al.*, Phys. Rev. C **64**, 024003 (2001).
108. A.B. Larionov, U. Mosel, Nucl. Phys. A **728**, 135 (2003).
109. FOPI Collaboration, in preparation.
110. H.H. Gutbrod *et al.*, Phys. Lett. B **216**, 267 (1989).
111. M. Demoulins *et al.*, Phys. Lett. B **241**, 476 (1990).
112. S. Voloshin, Y. Zhang, Z. Phys. C **70**, 665 (1996).
113. J.-Y. Ollitrault, preprint nucl-ex/9711003.
114. A.M. Poskanzer, S.A. Voloshin, Phys. Rev. C **58**, 1671 (1998).
115. S. Wang *et al.*, Phys. Rev. C **44**, 1091 (1991).
116. N. Borghini *et al.*, Phys. Rev. C **64**, 054901 (2001).
117. N. Borghini *et al.*, Phys. Rev. C **63**, 054906 (2001).
118. N. Borghini *et al.*, Phys. Rev. C **66**, 014905 (2002).
119. R.S. Bhalerao *et al.*, Nucl. Phys. A **727**, 373 (2003).
120. R.S. Bhalerao *et al.*, Phys. Lett. B **580**, 157 (2004).
121. N. Borghini *et al.*, Phys. Rev. C **66**, 014901 (2002).
122. M.B. Tsang *et al.*, Phys. Rev. Lett. **52**, 1967 (1984).
123. J.-Y. Ollitrault, Phys. Rev. D **48**, 1132 (1993).
124. W.K. Wilson *et al.*, Phys. Rev. C **45**, 738 (1992).
125. G. Fai *et al.*, Phys. Rev. C **36**, 597 (1987).
126. M.B. Tsang *et al.*, Phys. Rev. C **44**, 2065 (1991).
127. P. Danielewicz, Phys. Rev. C **51**, 716 (1995).
128. P. Danielewicz *et al.*, Phys. Rev. C **38**, 120 (1988).
129. J.-Y. Ollitrault, Nucl. Phys. A **590**, 561c (1995).
130. J.-Y. Ollitrault, Nucl. Phys. A **638**, 195c (1998).
131. S.A. Voloshin *et al.*, Phys. Rev. C **60**, 024901 (1999).
132. J. Barrette *et al.*, Phys. Rev. Lett. **73**, 2532 (1994).
133. M.M. Aggarwal *et al.*, Phys. Lett. B **403**, 390 (1997).
134. J. Łukasik *et al.*, in preparation.
135. J. Łukasik, W. Trautmann, in *Proceedings of the IWM2005 International Workshop on Multifragmentation and related topics, Catania, Italy, 2005*, edited by R. Bougault *et al.*, Conf. Proc., Vol. **91** (Italian Physical Society, Bologna, 2006) p. 387; preprint nucl-ex/0603028.
136. S.Y. van der Werf, Nucl. Instrum. Methods **153**, 221 (1978).
137. C.A. Ogilvie *et al.*, Phys. Rev. C **40**, 2592 (1989).
138. W.M. Zhang *et al.*, Phys. Rev. C **42**, 491 (1990).
139. P. Crochet *et al.*, Nucl. Phys. A **624**, 755 (1997).
140. B.-A. Li, A.T. Sustich, Phys. Rev. Lett. **82**, 5004 (1999).
141. M.B. Tsang *et al.*, Phys. Lett. B **148**, 265 (1984).
142. W.K. Wilson *et al.*, Phys. Rev. C **41**, R1881 (1990).
143. R.A. Lacey *et al.*, Phys. Rev. Lett. **70**, 1224 (1993).
144. P. Braun-Munzinger, J. Stachel, Nucl. Phys. A **638**, 3c (1998).
145. P. Danielewicz *et al.*, Phys. Rev. Lett. **81**, 2438 (1998).
146. J.-Y. Ollitrault, Phys. Rev. D **46**, 229 (1992).
147. S.A. Voloshin, Nucl. Phys. A **715**, 379 (2003).
148. F. Retière, J. Phys. G **30**, S827 (2004).
149. R.A. Lacey, Nucl. Phys. A **774**, 199 (2006); preprint nucl-ex/0510029.
150. The code IQMD was implemented at GSI by Y. Leifels (FOPI Collaboration), more results will be published elsewhere.
151. R. Kotte *et al.*, Eur. Phys. J. A **23**, 271 (2005).
152. S. Piantelli *et al.*, Phys. Lett. B **627**, 18 (2005).
153. G. Tabacaru *et al.*, Nucl. Phys. A **764**, 371 (2006).